Experiments in Fluids (2023) 64:30
https://doi.org/10.1007/s00348-023-03573-3

RESEARCH ARTICLE

Comparison of water and cryogenic fluid hammer experiments for rocket engine feed line systems

Sebastian Klein[1] · **Tobias Traudt**[1] · **Michael Oschwald**[1]

Received: 4 February 2022 / Revised: 28 November 2022 / Accepted: 23 December 2022 / Published online: 24 January 2023

Abstract

Fluid hammer occurs when a flow in a pipeline is rapidly stopped due to valve closure or shutting down a pump. The resulting pressure wave can reach very high amplitudes, depending on the fluid properties and the flow velocity. In spacecrafts and launchers, where the reduction of weight is always an important design goal, it is not possible to build the structure arbitrarily robust. Understanding the transient behaviour of the fluids is necessary to predict mechanical loads on the structure and align the design to them. Since a lot of launchers use reactive, cryogenic propellants, it is a common approach to use inert substitute fluids for on ground testing like water (H_2O) or liquid nitrogen (LN2). LN2 comes with the advantage of being cryogenic like real propellants, but ground testing is consequently more complex than with H_2O. For this purpose, several fluid hammer experiments with both fluids were performed and compared to each other to provide a foundation for deciding which substitute fluid would be useful.

Graphical abstract

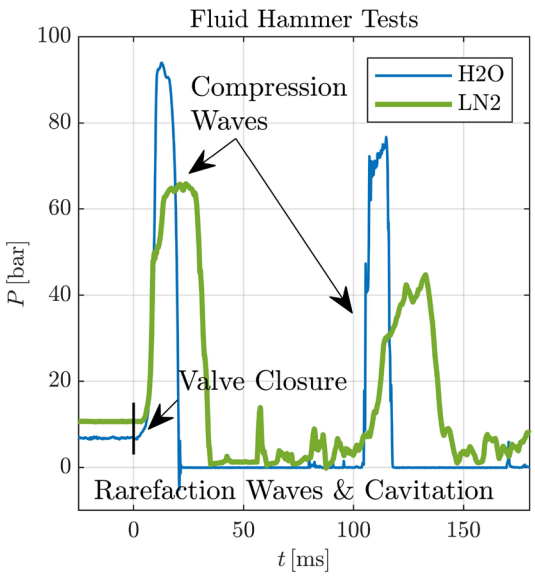

✉ Sebastian Klein
sebastian.klein@dlr.de

Tobias Traudt
tobias.traudt@dlr.de

Michael Oschwald
michael.oschwald@dlr.de

[1] German Aerospace Center, Institute of Space Propulsion, Langer Grund, 74239 Hardthausen, Germany

1 Introduction

Stopping a flow by closing a valve or shutting down a pump leads to high amplitude pressure waves, the so-called fluid hammer phenomena. The research of this effect goes back to the late 19th century, Joukowsky (1900) was one of the

first who derived the formula for the pressure rise if the flow is stopped instantaneous. A good overview about research activities with a focus on fluid hammer induced cavitation is given by Bergant et al. (2006).

Fluid hammer is a major problem in multiple fields and has been responsible for accidents like the destruction of a penstock at the Oigawa Power Station in 1950, which led to the death of three workers (Bonin 1960). In nuclear power plants the mixing of steam and cold water can lead to condensation induced water hammer (Barna et al. 2010). Since the resulting loads on the structure endanger the safety of the system, an accurate prediction of the loads is required to decide which components have to be replaced (Giot and Prasser 2004).

In mechanical heart prostheses, the occurrence of cavitation due to the water hammer can lead to potential damage of the valve itself or the blood components as suggested by Graf et al. (1991). A more recent study by Li et al. (2020) showed transient simulations of cavitation in a mechanical heart valve. In the field of rocket propulsion systems, a well-known example for fluid hammer is the loss of the 4th flight of the N1-L3 soviet lunar rocket. The shut down of an engine caused a shock wave which destroyed an oxygen pump (Lardier 2018). The Automated Transfer Vehicle, a spacecraft for logistic servicing the International Space Station, was tested with water as a substitute. Pressures of up to 220 bar were measured, this made it necessary to add a re-priming network to the spaceship (L'Hullier 2009). Fluid hammer tests with real propellants, like nitrogen tetroxide and hydrazine were performed by Gibek and Maisonneuve (2005).

A distinction is made between two types of fluid hammer test benches.

The *priming* setup contains an initially closed valve with pressurized liquid upstream and an evacuated pipeline with a dead end downstream. When the valve is opened, the pipeline is flooded by the liquid and hits the dead end, where a fluid hammer wave is created. The low pressure in the evacuated line and the associated high-pressure gradient across the valve cause the liquid to evaporate and the dead end to be hit by a two-phase flow. This setup was used with water and ethanol by Bombardieri et al. (2014) and with liquid nitrogen by Gouriet et al. (2016). They compared experimental results with Ecosim Pro/ESPSS simulations and called the code's prediction of flow questionable from a physical point of view.

In the *fluid hammer* setup, the fluid hammer is generated by stopping a stationary flow via closing a valve. The only publication using this setup and operating at cryogenic conditions known to the authors is the work of Joseph et al. (2017). They developed a one-dimensional transient flow model and compared it to experimental data of a 66 m long rocket engine feed line transporting liquid hydrogen. A fluid hammer wave is generated by closing the vent valve close to the engine at the end of the chill down process. They measured the fluid hammer pressure wave at an orifice 61 m downstream the tank and 5 m upstream the engine.

The Fluid Transient Test Facility at DLR Lampoldshausen was built to study the differences between water and cryogenic fluids in fluid hammer events with the occurrence of cavitation. This test facility can be used with either the *priming* configuration or the *fluid hammer* configuration. Previous work with water focused on different topics, like flow visualization (Traudt et al. 2015), influences on the damping behaviour (Klein et al. 2018, 2019) and the cavitation as an acoustic boundary condition (Klein et al. 2020).

In this paper, experimental data from the *fluid hammer* setup with liquid nitrogen over a wide pressure range are presented and then compared to equivalent experiments with water. This work is a contribution to extend literature with experimental data of cryogenic fluid hammer by stopping a stationary flow. The main focus is on the first pressure peak after valve closure and the occurrence of cavitation close to the valve immediately afterwards. Furthermore, the presented data can be used as a test case for validation of numerical models.

2 Theory

The basic principle of fluid hammer is explained in Fig. 1, a tank is connected through a pipeline to a valve. The setup is shown at eight points in time. Before t_1 the valve is open and the pressure inside the pipe is $P = P_0$. At time $t = t_1$ the valve is closed while the fluid is flowing with the velocity v. The fluid is then stopped immediately and a compression wave with pressure P_1 travels with the speed of sound a towards the tank, which is reached at $t = t_2$. The velocity behind this compression wave is $v' = 0$. At $t = t_3$ the wave is reflected at the tank and is then travelling towards the valve ($t = t_4$). The compression wave is reflected as a rarefaction wave at the valve. Now the flow direction is changed and the fluid flows back into the tank with the pressure $P = P_0$ behind the rarefaction wave.

At $t = t_5$ the wave is reflected at the valve, where it surpasses P_0 and is then travelling towards the tank at $P = P_{1'}$ ($t = t_6$). The wave is reflected at the tank ($t = t_7$), which leads to another change in the flow direction. Finally the compression wave is going back towards the valve ($t = t_8$), when it hits the valve the same condition as at $t = t_1$ is reached. The rarefaction wave is reflected as a compression wave; therefore, the fluid hammer cycle starts again.

The rise in pressure $\Delta P = P_1 - P_0$ can be calculated by the Joukowsky equation, the fundamental equation of water hammer:

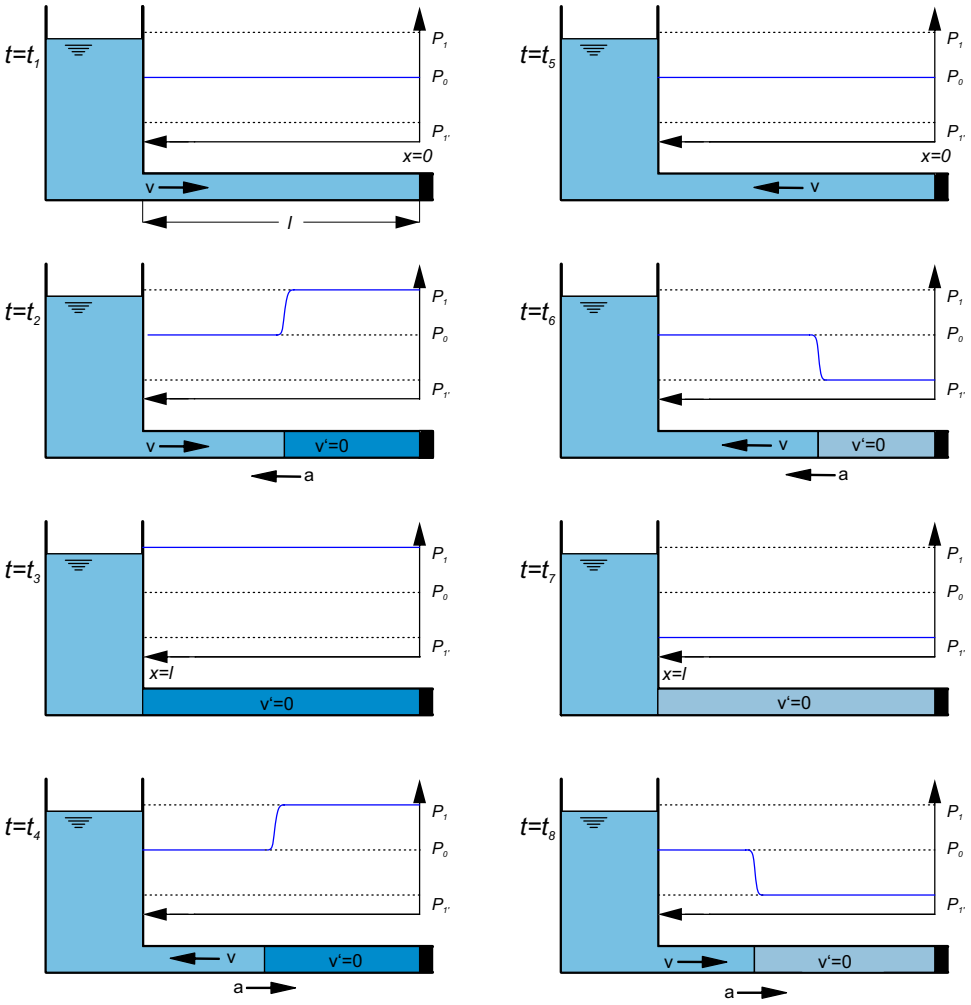

Fig. 1 Schematic of the fluid hammer oscillation in a pipeline after rapid valve closure

$$\Delta P_{\mathrm{Jou}} = \pm \rho a \Delta v \tag{1}$$

Where ρ is the density of the fluid, a the speed of sound of the fluid and Δv is the change of the flow velocity. Because the flow is completely stopped, the change in velocity equals the flow velocity at valve closure: $\Delta v = v_0$. To compare two different fluids, it is necessary to know what pressure increase can be achieved per flow velocity. The product of ρa is shown for different pressures versus temperature in Fig. 2 for water and liquid nitrogen. The temperature range is selected around the respective operating condition with $\pm 10\,\mathrm{K}$. The absolute ρa values for H_2O are about double as high as ρa for LN2, while the derivative with respect to temperature is an order of magnitude greater for LN2 than for H_2O.

As described by Korteweg (1878), the sound velocity of the fluid in a pipe is reduced when the elasticity of the

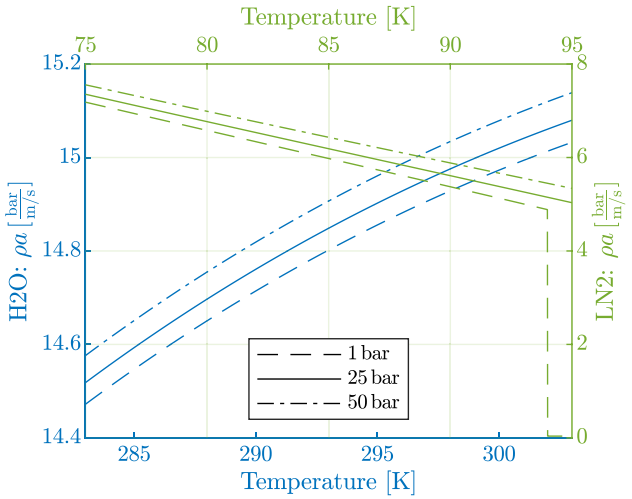

Fig. 2 Joukowsky pressure: pressure rise per flow velocity for H_2O and LN2 for several operating conditions

tube is comparable to the elasticity of the fluid flowing through it.

$$a = \sqrt{\frac{K/\rho}{1 + [(K/E)(D/e)]c_1}} \tag{2}$$

This reduction can be calculated knowing the fluids bulk modulus K and pipe properties such as the Young modulus E, the inner diameter D and the wall thickness of the pipe e. For thick-walled pipes ($D/e < 25$), which are anchored against longitudinal movement, the factor c_1 is a function of the pipe's geometry and the Poisson coefficient ν (Wylie et al. 1993).

$$c_1 = \frac{2e}{D}(1+\nu) + \frac{D(1-\nu^2)}{D+e} \tag{3}$$

Since the pressure wave passes through the pipe four times per oscillation the frequency of the oscillation f can be calculated as

$$f = a/4l \tag{4}$$

which corresponds to the first eigenfrequency ($n = 1$) of a tube with one end open and one end closed (oc).

To calculate higher eigenfrequencies ($n > 1$) in an open-close tube, a pre-factor is used as shown in Eq. 5:

$$f_{\mathrm{oc}}(n) = (2n-1) \cdot \frac{a}{4l} \tag{5}$$

Neglecting the damping of the system, the pressure in the first wave trough $P_{1'}$ decreases by the same amount as P_1 increases from P_0. If the absolute value of $\Delta P_1 = P_1 - P_0$ is bigger than $P_0 - P_v$, the pressure behind the fluid hammer wave drops to P_v and cavitation occurs close the valve. This case is shown schematically in 3. A major difference to fluid hammer without cavitation is that the velocity behind the pressure wave v' is not reduced to zero but to

$$v'(t = 2l/a) = v_1 = v - \frac{P_0 - P_V}{\rho a}. \tag{6}$$

The right term represents the decrease in flow velocity due to the pressure drop from P_0 to P_V. As shown in Fig. 3, the fluid hammer wave is oscillating between the reservoir and the cavity. The cavity acts as a boundary condition and the velocity $v'(t)$ is reduced by $2(P_0 - P_V)/(\rho a)$ every time the wave is travelling through the pipe back and forth ($2L/a$). Consequently, at a certain point in time the flow direction changes towards the valve (Bergant et al. 2006). Wylie et al. (1993) used this behaviour to estimate the duration of the first cavity till it collapses, see Eq. 13.

Several forms of cavitation, depending mainly on the slope of the pipe and the resulting change in static pressure

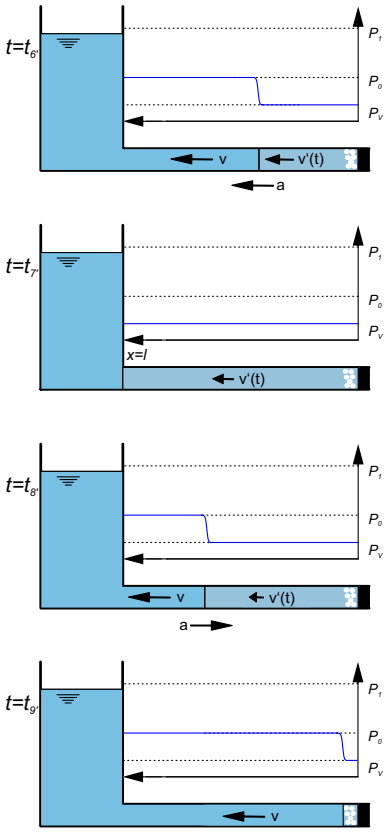

Fig. 3 Schematic of the fluid hammer oscillation in a pipeline while cavitation

are presented by Zielke and Perko (1985) and has been adapted by Bergant et al. (2006). An increasing inclination towards the valve favours the occurrence of column separation, while no inclination at all leads to column separation close to the valve with distributed cavitation next to it (Bergant et al. 2006). Since the first meter upstream of the valve at the used test section is horizontal, it is important to know the density and speed of sound in an area containing a vapour–liquid mixture.

The density, as a function of void fraction $\chi = V_g/V_m$, where V_g is the gas volume in proportion to the total volume of the mixture V_m, the density in liquid phase ρ_l and in gaseous phase ρ_g is given by

$$\rho(\chi) = \rho_g \cdot \chi + (1-\chi) \cdot \rho_l\,. \tag{7}$$

To calculate the speed of sound in a two-phase flow a_{2p}, the Wood equation, presented by Wilson and Roy (2008) is used.

$$\frac{1}{a_{2p}^2} = \frac{(1-\chi)^2}{a_l^2} + \frac{\chi^2}{a_g^2} + \chi(1-\chi)\frac{\rho_g^2 a_g^2 + \rho_l^2 a_l^2}{\rho_l \rho_g a_l^2 a_g^2} \tag{8}$$

Here, the speed of sound in liquid phase a_l and in gaseous phase a_g are taken into account.

The acoustic impedance is the product of the speed of sound a and the density ρ,

$$Z = \rho \cdot a. \tag{9}$$

A pressure wave moving through a fluid is reflected and transmitted when it hits a different medium or phase with different acoustic impedance. The reflection coefficient R for a wave travelling vertically from one medium to another is described by Skudrzyk (2012).

$$R = \frac{\zeta + 1}{\zeta - 1} \tag{10}$$

The ratio of the acoustic impedances at the media interface is expressed by $\zeta = Z_2/Z_1 = \rho_2 c_2/\rho_1 c_1$.

The reflection coefficient R of a wave propagating from a liquid area to a two-phase area with the void fraction χ is given in Fig. 4. In both fluids, R decreases from $R(\chi = 0) = 0$ (liquid → liquid) to $R(\chi = 1) = -1$ (liquid → gas), with the sharpest decrease a the beginning. This effect is more prominent in H_2O than in LN2.

The cavitation close to the valve replaces the valve as an acoustic boundary condition. Since $R = -1$ indicates an open end boundary condition, the system is changing towards being open at both ends (oo) where the eigenfrequencies f_{oo} are calculated as follows:

$$f_{oo}(n) = n \cdot \frac{a}{2l} \tag{11}$$

Comparing Eqs. 5 and 11 it becomes apparent that $f_{oo}(n = 1)$ is twice the frequency of $f_{oc}(n = 1)$ and the difference between the overtones $\Delta f = f(n + 1) - f(n)$ is the same: $\Delta f_{oc} = \Delta f_{oo}$.

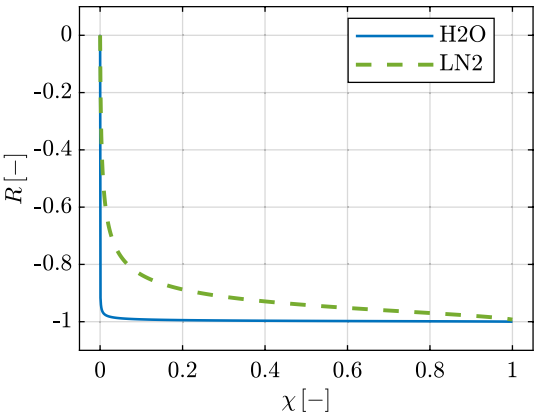

Fig. 4 Reflection coefficient R as a function of χ for an acoustic wave propagating from a liquid into a two-phase region. Temperatures: $T_{H2O} = 298$ K, $T_{H2O} = 87$ K

3 Fluid transient test facility

The Fluid Transient Test Facility (FTTF) was built in two configurations, both shown in Fig. 5. The water configuration (FTTF-1) is described in detail in the work of Traudt et al. (2016), the cryogenic configuration (FFTF-2) was built according to its design. Both configurations include two similar pressurized tanks (HP and LP) connected by a pipeline (test section), all made of stainless steel of grade 1.4541. In both configurations gaseous nitrogen is used to pressurize the tanks. A Coriolis flow meter and a fast closing axial valve are used. The test section is equipped with three sensor positions (S1, S3, S2 or S4), each position contains a static pressure sensor (FTTF-1: Kistler 4043A-100, FTTF-2: Kulite CTL-190 S-2000A), a dynamic pressure sensor (Kistler 601) and a type K thermocouple.

The dynamic and static pressure sensors are mounted flush with the wall, the tip of the thermocouple is in the centre of the flow. The term *dynamic* refers to the behaviour of the sensor, which can only measure relative pressure changes. In the event of a permanent pressure change, the measured value falls back to zero over time.

The sampling frequency f_s, the anti-aliasing frequency f_{AA} and range of the sensors are given in Table 1. Unless otherwise specified, the pressure values given are measurements with static pressure sensors: $P_{S1..S4}$.

The measurement chain is shown schematically in Fig. 6. Both, pressure and temperature signals are amplified and split by an AS4 - amplifier. The DAQ (data acquisition) system is responsible for saving the data, while the Werum

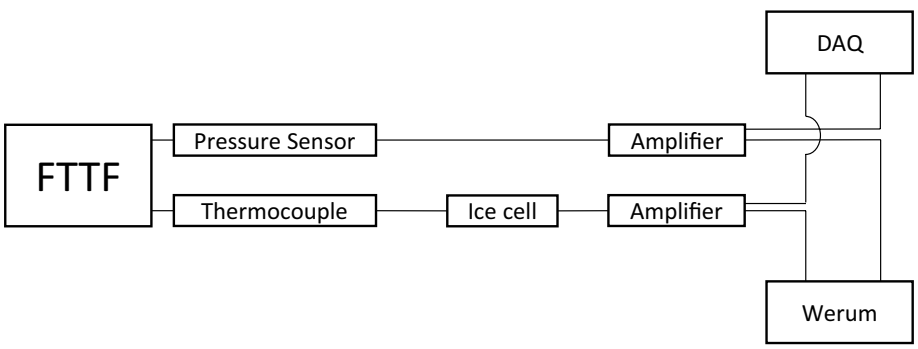

Fig. 5 Fluid Transient Test Facility (FTTF): H_2O configuration(left), LN2 configuration (right)

Table 1 Sensors of the test benches FTTF -1/2

Model	f_s	f_{AA}	Range	FTTF
Kistler 4043A-100	10 kHz	30 kHz	0 – 100 bar	1
Kulite CTL-190 S-2000A	10 kHz	2 kHz	0 – 100 bar	2
Kistler 601	150 kHz	2 kHz	0 – 250 bar	1 & 2
Thermocouple Type K 0.5 mm tip	100 Hz	200 Hz	−200 – 40 K	1 & 2

Table 2 Dimensions of the test bench FTTF -1/2

Parameter		FTTF-1	FTTF-2
Max. tank pressure	P_{HP},P_{LP}	50 bar	50 bar
Max. peak pressure	P_{max}	100 bar	100 bar
Max. mass flow	$\dot{m}$	1.74 kg/s	2.8 kg/s
Tank volume	V_{HP},V_{LP}	80 l	80 l
Pipe length	l	7.67 m	9.29 m
Pipe inner diameter	d	19 mm	19 mm
Pipe wall thickness	e	1.5 mm	1.5 mm
Sensor position 1	x_1/l	3.9 %	6.46 %
Sensor position 2	x_2/l	–	47.3 %
Sensor position 3	x_3/l	88.8 %	88.2 %
Sensor position 4	x_4/l	97.8 %	–

system is used to control the test bench. The measurement error of the system is the sum of the sensor error, the amplifier error and the DAQ error. The DAQ error is < 0.002%, the amplifier error is 0.5% and the pressure sensor error is < ±50 mbar. The error of the thermocouple depends on the temperature, it is ±2.5 K in cryogenic conditions and ±1.5 K at ambient temperature.

Thanks to the experience gained with the FTTF-1, sensor positions for the FTTF-2 have been optimized. It was observed that the pressure signals at position S3 and S4 were very similar to each other, the use of both did not generate any added value. Therefore the sensors of position S4 were moved to position S2, which gives more insight on the pressure waves moving through the test section. Since both configurations use the same data acquisition system, the number of sensors is set.

Since the FTTF-2 is designed for cryogenic purposes, an adequate isolation must be ensured. Both tanks are enclosed by a jacket containing LN2 in saturation state at near ambient pressure to eliminate heat input from the environment into the tanks. The pressure in the jacket is slightly higher than ambient pressure due to the use of a check valve with an opening pressure of < 0.3 mbar. The test section is a one and a half spiral inclined by 0.62° towards the valve. A vacuum isolation is used to reduce heat entrance from the environment. The valve of type Axius 1400 S is closing within $\Delta t_{valve} = 18$ ms and is located upstream of the Coriolis flow meter (Emerson CMF50M). Foam isolation is used to minimize the heat entrance into the valve.

The dimensions of the test bench are given in Table 2. The main difference between both configurations is the length of the pipe, the FTTF-2 pipe is 1.62 m longer than the FTTF-1 pipe, inner diameter and wall thickness are the same. To achieve good comparability between both configurations the relative sensor positions x_1/l and x_3/l are at similar positions in both configurations.

Several steps are required to chill down the test bench before starting with test activities, these steps are presented in the following:

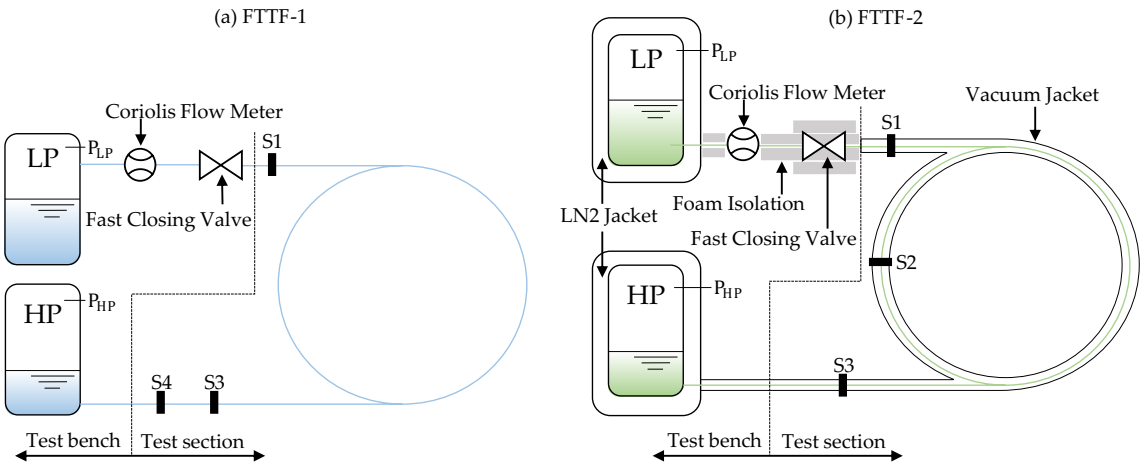

Fig. 6 Fluid Transient Test Facility (FTTF): Measurement technique

Table 3 Datasets: H_2O & LN2

Parameter	H_2O	LN2
Number of reference test cases	26	30
Number of test cases with cavitation	230	140
Range of P_0 [bar]	1.2 – 47.5	2 – 43.4
Range of T_0 [K]	289.8 – 295.3	84.5 – 112.2

Chill down

- Purging of the tanks, Coriolis flow meter, valve and test section with gaseous nitrogen.
- Filling of the jackets with LN2.
- Filling of the LP tank with LN2.
- Moving the fluid from the LP tank to the HP tank and back about 10 times to chill down the test section.

When the test bench is cold, each test follows the same procedure. Between tests the fluid is pumped from the HP tank towards the LP tank and back to ensure a homogeneous temperature in the test section.

Test procedure

- Filling of the HP tank with LN2.
- Closing the valve and pressurize both tanks to the desired pressure.
- Open the valve to create a flow from the HP tank towards the LP tank.
- Stop the flow by closing the valve rapidly after a stationary flow has formed.
- Measure the fluid hammer in the test section until the oscillation has subsided.

4 Experimental results

Two datasets were created to compare H_2O and LN2 fluid hammer. Both sets are divided into cases with cavitation and reference cases without cavitation. The amount of test cases and the pressure, and temperature range before valve clothing can be found in Table 3. Subsets of the datasets have been used in previous work, the H_2O set in reference (Klein et al. 2018, 2019, 2020) and the LN2 set in reference (Klein et al. 2021).

Six test cases are used in this work as examples. Their boundary conditions at valve closure $t_0 = 0$ ms are listed in Table 4.

Two LN2 test cases, one without cavitation (case A), one with cavitation (case B) are presented in detail. First, an overview of the most important parameters over the entire sequence period for test case B is given in Fig. 7. Then, the pressure readings in the test section (P_{S1}, P_{S2}, P_{S3}) after valve closure are displayed in Figs. 8 and 9.

Mass flow $\dot{m}$, Temperature T_{S1} and the pressure in both vessel (P_{HP}, P_{LP}) and at position S1 (P_{S1}) are presented from

Table 4 Boundary conditions of all test cases presented

	Case A	Case B	Case C	Case D	Case E	Case F
Medium	LN2	LN2	LN2	LN2	H_2O	H_2O
$P_{HP,0}$ [bar]	26.47	13.94	8.62	8.59	13.7	8.56
$P_{LP,0}$ [bar]	21	1.79	6.25	6.02	10.4	1.11
T_0 [K]	91.1	86.79	84.9	86.1	293.94	295.08
$\dot{m}_0$ [kg/s]	1.12	1.94	1.45	1.43	1.12	1.78
v_0 [kg/s]	5.3	8.94	1.45	1.43	3.96	6.29

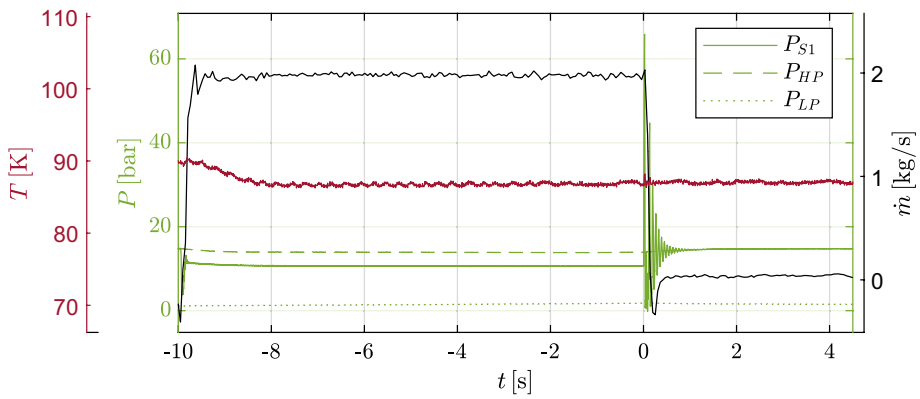

Fig. 7 LN2 - case B: Overview

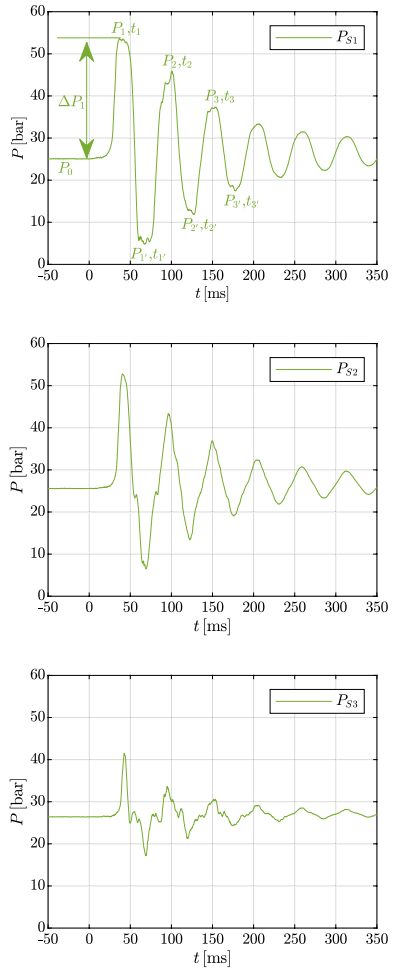

Fig. 8 LN2 - case A: Pressure traces of a fluid hammer without cavitation

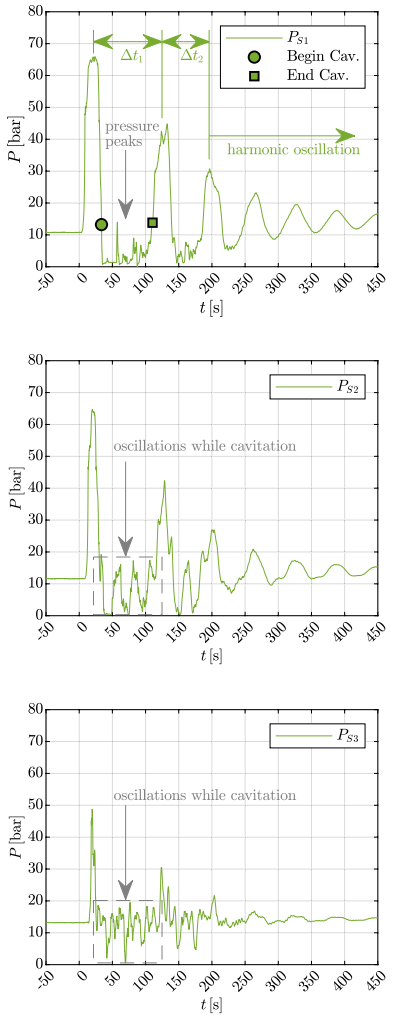

Fig. 9 LN2 - case B: Pressure traces of a fluid hammer with cavitation

the initial valve opening $t = -10$ s till the end of measurement at $t = 4.5$ s. The pressure traces, the temperature T_{S1} and $\dot{m}$ reach a stationary level 2 s after valve opening. The valve is closed at $t = 0$ s and the fluid hammer occurs.

The pressure traces (P_{S1}, P_{S2}, P_{S3}) of a non-cavitation test (case A) are presented in Fig. 8. A damped pressure oscillation can be seen at all three sensor positions. The pressure before valve closing at sensor position S1 is P_0, the pressure peaks are labelled as P_1, P_2 … P_n at the corresponding time $t_1, t_2..t_n$. Negative pressure peaks at the wave troughs are named $P_{1'}, P_{2'}..P_{n'}$ at time $t_{1'}, t_{2'}..t_{n'}$. The time between each peak is given by $\Delta t_i = t_{i+1} - t_i$, while the amplitude is given by $\Delta P_i = P_i - P_0$.

A detailed look at the fluid hammer pressure traces from case B is given in Fig. 9. The periods of wave troughs with cavitation are longer than the ones without and $\Delta t_1 > \Delta t_2$. Ideally, P_{S1} would remain at the level of the vapour pressure during the occurrence of cavitation, however, an increase in P_{S1} is observed at the end of the cavitation valley. The pressure peaks in the first cavitation valley in P_{S1} and the pressure oscillations in P_{S2} and P_{S3} will be analysed in chapter 5. After the last valley with cavitation, a harmonic damped oscillation can be seen, comparable to case A (Fig. 8). The beginning of the harmonic oscillation is defined as the first pressure peak P_n after which the vapour pressure in the prior valley is no longer undershot.

4.1 Reproducibility

As the test bench has to be chilled down again every test day, achieving test reproducibility is an important challenge in order to obtain valid information. Therefore several tests have been repeated at two different test days to verify the procedures mentioned in chapter 3. The results of one of these repeated tests (cases C & D) are shown as an example in Fig. 10. The main input parameters at valve closing are presented in Table 4.

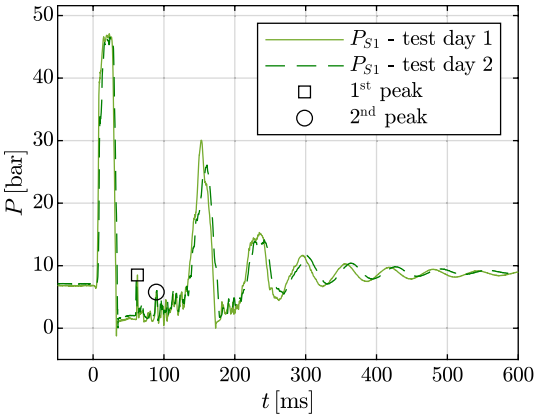

Fig. 10 LN2: Repeating the same experiment on two test days to show reproducibility

Since the closing of the valve always varies by a few milliseconds, the pressure curves are shifted in time as if the valve opening would have happened at the same time. P_0 of both tests is around 8.6 bar and both tests reach a maximum pressure of around $P_1 = 46$ bar. Both cases show a very similar behaviour, especially the good agreement of the pressure waves during cavitation should be emphasized.

First, the pressure in the first wave trough is almost constant, after about 27 ms a sharp pressure peak can be observed. The second pressure peak, approximately 27 ms after the first one is only faintly visible, because more and more pressure fluctuations occur at the end of the cavitation valley. This time period is as large as the width of the first pressure peak of the fluid hammer wave.

A comparison of P_{S1} in both fluids is given in Fig. 11. The amplitudes are comparable to each other. With respect to the different size of ρa (see Fig. 2), v_0 of case B is about twice as large as in case E. Although the frequencies of the test cases differ, due to differences in a and l, the decrease in amplitude is comparable. While cavitation, the pressure drops on vapour pressure, which is significantly lower in H_2O than in LN2. When comparing the measured pressure during cavitation with the vapour pressure, it must be noted that the measured pressure is subject to measurement error and the vapour pressure is calculated based on a measured temperature. Temperature measurement is also affected by measurement error, which is greater in a cryogenic environment than at ambient temperature. During this period, the pressure is nearly constant in H_2O with a clearly defined beginning and ending. In LN2, on the other hand, pressure fluctuations were observed and the pressure in both cavitation valleys rises towards the end.

4.1.1 Pressure losses

To determine the pressure loss of the pipeline as a function of the flow velocity, the pressure at position S3 (LN2) $P_{0,S3}$, respectively, S4 (H_2O) $P_{0,S4}$ is measured and compared to the pressure at position S1 $P_{0,S1}$. All values are measured right before valve closure ($t_0 = 0$ ms). These pressure differences versus the associated v_0 are given in Fig. 12, where each data point represents an individual test case.

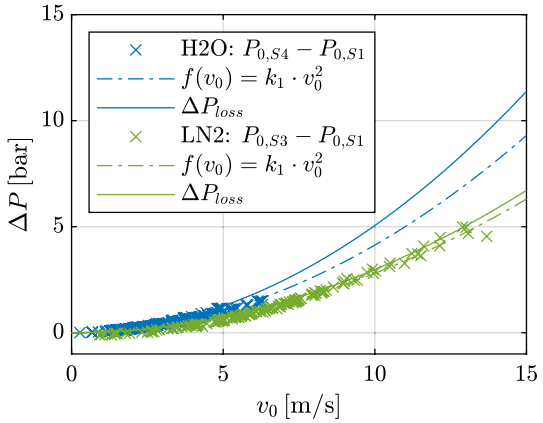

Fig. 12 H_2O/LN2: Pressure losses in stationary flow, before valve closure

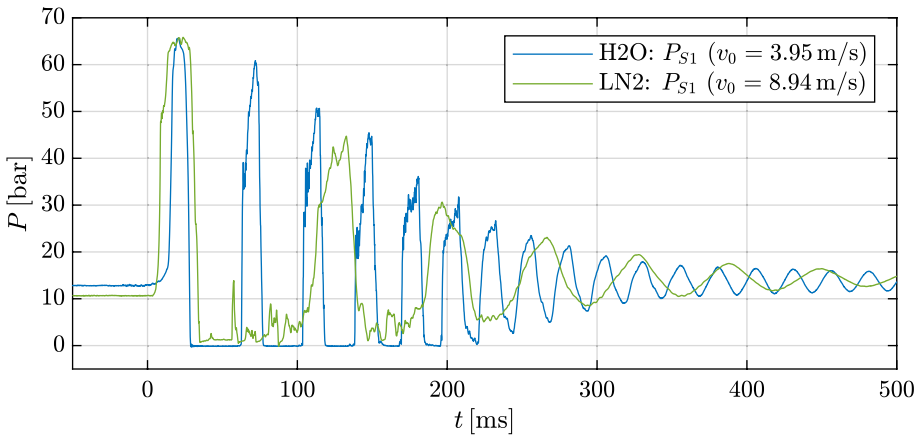

Fig. 11 H_2O/LN2: Pressure traces at position S1

Table 5 Fit parameters k_1, k_2 and coefficient of determination r^2

Medium	k_1	k_2	r^2
H2O	4134	1/0.939	97.35 %
LN2	2801	1/0.8174	98.81 %

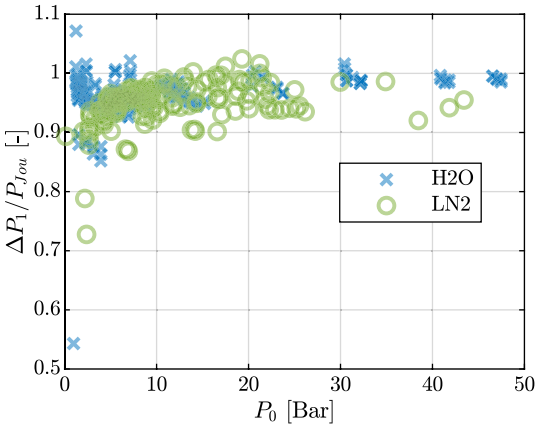

Fig. 13 H_2O/LN2: Comparison of the measured first pressure peak with the Joukowsky pressure

The relationship between pressure loss and v_0 is expressed by a first grade polynomial fit function $f(v_0) = k_1 \cdot v_0^2$, the fitting parameter k_1 and r^2 are given in Table 5. Since these pressure sensors does not cover the whole length l, the factor k_2 is added, which is the ratio between the distance between sensor positions and the length of the test section:

$$\Delta P_{\text{loss}} = (k_1 \cdot v_0^2) \cdot \frac{l}{x_{3;4} - x_1} = (k_1 \cdot v_0^2) \cdot k_2 \tag{12}$$

4.2 Comparison to theoretical solutions

In this chapter the experimental data sets will be compared with theoretical solutions from chapter 2.

4.2.1 Joukowsky

First, the measured amplitude ΔP_1 is compared to the Joukowsky pressure ΔP_{Jou}, shown in Eq. 1. The ratio $\Delta P_1/P_{Jou}$ over P_0 is presented for H_2O and LN2 in Fig. 13. For both substances most cases show a good agreement with the Joukowsky pressure: $\Delta P_1/P_{Jou} > 0.9$. While for H_2O no dependency on P_0 was observed, for LN2 it can be seen that the agreement with the Joukowsky pressure decreases for small P_0.

4.2.2 Frequency

Next, the frequency of the harmonic oscillation is compared to the theoretical solution from Eq. 5. The speed of sound a for both fluids is calculated using Eq. 2. For reference cases without the occurrence of cavitation, a FFT was applied on the entire pressure signal. The most excited frequency f_{exp} is compared with the theoretical solution f_1 from Eq. 4. Test cases with the occurrence of cavitation are analysed the same way, with the restriction that only the harmonic part after a threshold of 100 ms of the signal is taken into account (see Fig. 9). Only test cases with an amplitude of more than 10% of the terminal pressure are considered for this analysis.

In Fig. 14, the deviation from the analytical eigenfrequency in water experiments is shown in a histograms with a bin width of 2.5%. The reference test cases are presented in Fig. 14a. The vast majority of all measured frequencies show a matching of 95 – 97.5% of the calculated value. In

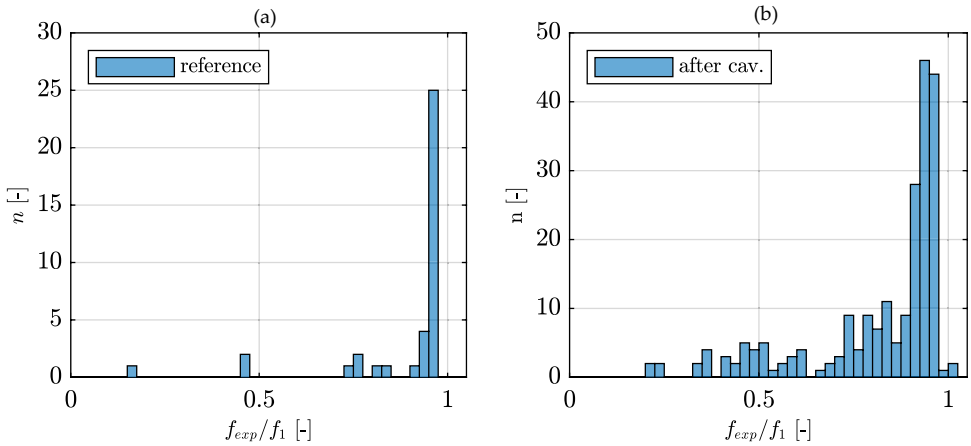

Fig. 14 H_2O: Ratio of the measured frequency f_{exp} to the calculated frequency f_1. **a** Reference test cases without cavitation. **b** Test cases with occurrence of cavitation

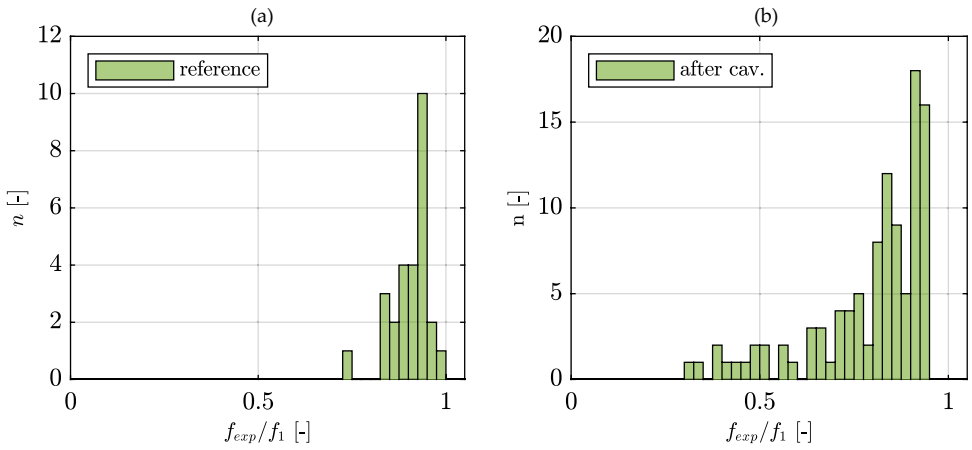

Fig. 15 LN2: Ratio of the measured frequency f_{exp} to the calculated frequency f_1. **a** Reference test cases without cavitation. **b** Test cases with occurrence of cavitation

Fig. 14b, test cases with occurrence of cavitation are shown. The deviation of measured frequencies from the theoretical frequency is much wider in comparison to the reference cases.

Figure 15 shows the distribution from the theoretical frequency for tests performed with LN2. The deviation of the measured frequency in reference cases in LN2 is much broader than in H_2O tests. Most measured frequencies f_{exp} are $92.5 - 95\%$ of f_1. In the test cases with cavitation, an exponential distribution of f_{exp}/f_1 can be seen, with the maximum at $0.9 - 0.925\%$.

A possible explanation for this deviation is a reduction of the speed of sound, which could be caused by the presence of gas or vapour. Dissolved gas is released from a fluid as a result of pressure drop within milliseconds, but gas absorption is in order of minutes (Bergant et al. 2006). For H_2O experiments, which are pressurized by gaseous nitrogen, it is likely that a small amount of dissolved gas remains in the fluid. To ensure the same amount of gas on each test day, the fluid was stored over night at 1 bar. This dissolved gas is released during pressure oscillations and is then lowering the speed of sound of the fluid. Since liquid nitrogen is pressurized with gaseous nitrogen, this effect is excluded as a possible cause. The purity of the used LN2 is given with $\geq 99.999\%$.

4.2.3 Cavitation duration

To analyse the duration of the first cavitation valley Δt_c, start time and end time of the cavitation duration must be specified. The start time is set at the moment when P_{S1} crosses P_{S3} for the first time after first pressure peak. Analogously, the end time is set as the moment at which P_{S1} crosses P_{S3} before the second pressure peak. Start and end time of case B are marked in Fig. 9. The length of the first cavitation valley is compared to the estimated cavitation time Δt_c by Wylie et al. (1993) which is given in Eq. 13.

$$\Delta t_c = A_{\text{rel}} \cdot \frac{2l}{a} = \frac{P_1 - P_0}{P_0 - P_v} \cdot \frac{2l}{a} \tag{13}$$

According to Wylie et al. (1993), the duration of cavitation is the time needed by the pressure wave to travel back a fourth through the pipe ($2l/a$) multiplied with the relative amplitude A_{rel}, which is the ratio between the fluid hammer pressure rise $\Delta P_1 = P_1 - P_0$ and the pressure difference $P_0 - P_v$.

A different method to estimate the cavitation duration and expansion is to solve differential equations for the movement of the liquid column in the pipeline (Prasser et al. 1998). For this purpose, it is assumed that the cavitation zone fills the whole cross section of the pipe and has a sharp border with the liquid column, where compressibility effects are neglected. The left side of Eq. 14 is the movement of the liquid column, x_c is the spatial expansion of the cavitation zone. The back pressure of the tank HP is given by P_{HP} and the pressure losses ΔP_{loss} are experimentally determined, see Fig. 12. The reduced friction due to change of the length of the fluid column is taken into account by multiplying ΔP_{loss} with $(l - x_c)/l$.

$$\rho_l \cdot (l - x_c) \cdot \frac{\mathrm{d}v}{\mathrm{d}t} = P_v - P_{\text{HP}} - \Delta P_{\text{loss}} \cdot \frac{l - x_c}{l} \tag{14}$$

The spatial expansion x_c can be calculated by integrating the flow velocity v over time t.

$$x_c = \int_0^t v \cdot \mathrm{d}t \tag{15}$$

To solve these equations, initial conditions for x_c and v must be set. The calculation starts at the moment when the rarefaction wave leaves the valve in the direction of the tank, therefore: $x_c(t = 0) = 0$ and $v(t = 0) = v_1$ (see Eq. 6).

The result for case E are shown in Fig. 16, respectively, for case B in Fig. 17. Besides x_c, the pressure traces P_{S1} and P_{HP} are displayed. In both test cases x_c has a parabolic form and a maximum expansion of $\approx 13\,\text{cm}$. The calculation is

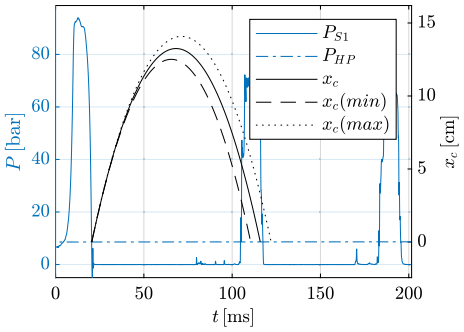

Fig. 16 H2O case E: Spatial expansion of the gaseous area

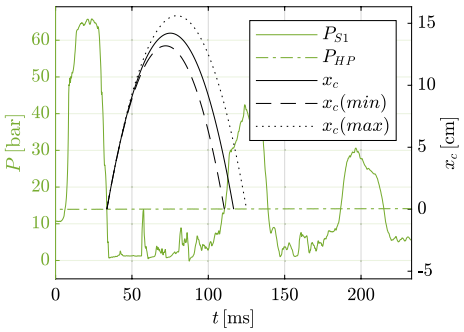

Fig. 17 LN2 case B: Spatial expansion of the gaseous area

stopped when x_c reaches negative values, consequently the modelled lifespan of the cavitation $\Delta t_{\mathrm{c,model}}$ is the whole calculation period. In both cases the duration is overestimated by the model.

Since the input parameters P_v and P_{HP} are measured values, the measurement errors $\Delta P_{\mathrm{error}}$, $\Delta T_{\mathrm{error}}$ must be taken into consideration. To calculate the minimal gas expansion $x_c(\mathrm{m}in)$, P_v is calculated at $T_0 - \Delta T_{\mathrm{error}}$ and the tank pressure is $P_{\mathrm{HP}} + \Delta P_{\mathrm{error}}$. The maximum expansion $x_c(\mathrm{m}ax)$ is calculated vice versa.

The estimated cavitation durations by the methods of Wylie et al. (1993) and Prasser et al. (1998) are compared to experimental data, the results are shown in Fig. 18. The measurement errors $\Delta P_{\mathrm{error}}$, $\Delta T_{\mathrm{error}}$ are also considered for the Wylie method. In general, the prediction with the Prasser method is more accurate than the prediction with the Wylie method. $\Delta t_{\mathrm{c,model}}/\Delta t_{\mathrm{c,exp}}$ in both fluids is increasing with increasing v_1 and the cavitation duration is overestimated up to factor 2. A better match is achieved with the Prasser model, in H_2O the model approaches a value of $\Delta t_{\mathrm{c,model}}/\Delta t_{\mathrm{c,exp}} = 1.3$ for increasing v_1. In LN2 it can be seen that the matching is nearly perfect for increasing v_1. Furthermore, it must be emphasized that the error decreases for increasing v_1. In H_2O, there is a group of outliers where the duration is predicted to be much longer compared to the experimental data. The reason for this behaviour remains unclear but these are the data of one test day. At low v_1, large downward deviations are observed in both fluids. These low initial flow velocities are only possible if P_v is only slightly undershot. Therefore it is possible that in these cases column separation is not formed.

The formulation of the Prasser model used in this analysis did not cover any unsteady friction effects. The implementation of this term in future work could enhance the accuracy of the model.

As shown in Fig. 2, ρa is much bigger in H_2O than in LN2, therefore v has to be higher in LN2 in order to create comparable ΔP_1. High flow velocity requires big pressure difference between both tanks, which results in higher P_0. This effect reduces A_{rel} in LN2 cases, however P_V is much higher in LN2 than in H_2O, which decreases $\Delta P_{1'}$ and leads to increasing A_{rel}.

4.2.4 Attenuation

Since the fluid hammer is a damped harmonic oscillation, another parameter of interest is the decay constant δ. It is calculated for the reference test cases and the harmonic part of the cavitation test cases. Independently of the fluid hammer, the valve closure results in a pressure rise to P_{HP} in the pipeline. To separate the attenuation of the fluid hammer from this effect P_{HP} must be subtracted from P_{S1}: $\hat{P} = P_{S1} - P_{HP}$. The pressure trace $\hat{P}$ is then shifted in time, so that first pressure peak of the harmonic oscillation is at $t = 0$ ms. The quality of the fit is given by r^2, which is $r^2 > 95\%$ in 96% of test cases in both fluids. For case B, the results of this method are shown in Fig. 19.

The results for H_2O and LN2 are given in Fig. 20. The decay constants for both fluids appear to be in the same order of magnitude. In H_2O δ is increasing with increasing P_0 for non-cavitation cases. The scattering of δ in cavitation cases is decreasing with increasing P_0. The scatter of the LN2 cavitation cases is even bigger than for H_2O. In contrast to water, δ varies strongly, even for test cases without cavitation.

5 Cavitation as an acoustic boundary condition

The occurrence of cavitation close to the valve leads to a local reduction of the density and speed of sound and therefore to a reduced acoustic impedance in this area. As shown in Fig. 4, the reflection coefficient approaches $R = -1$ with increasing χ. In previous work with H_2O it was shown that it is likely for the cavitation to act as an open end boundary condition but the pressure wave could not be tracked directly

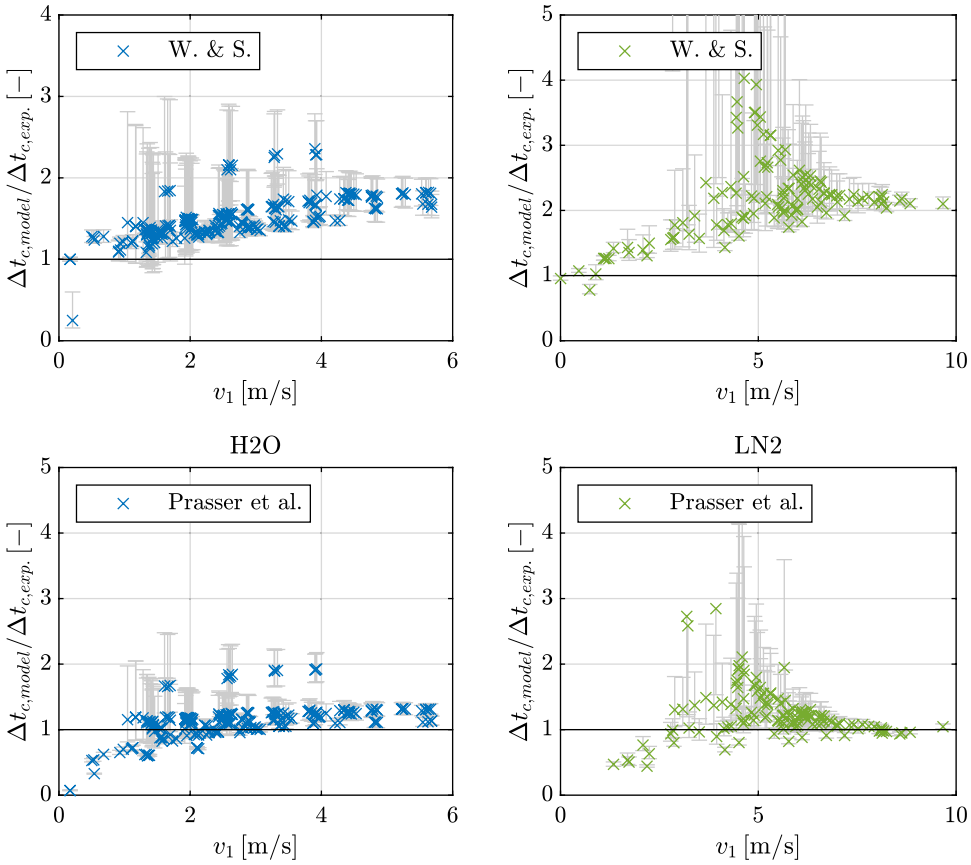

Fig. 18 H_2O, LN2: Agreement of the models with experimental data

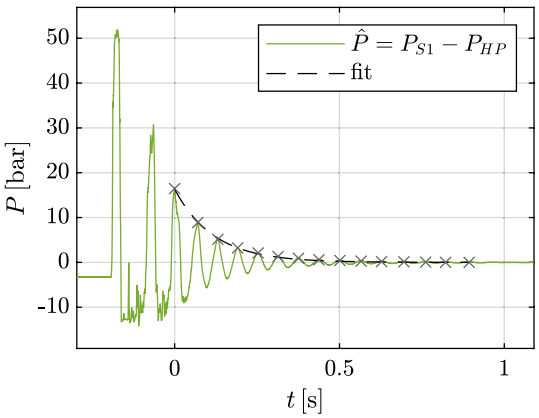

Fig. 19 LN2 - case B: Exponential fit of the harmonic part of the oscillation

(Klein et al. 2020). The presented experimental water data deviated from the theory presented in Fig. 3.

To compare the acoustic behaviour in LN2 with that in H_2O, the method used by Klein et al. (2020) is applied to the LN2 data set. The following is a brief explanation of the method, a more detailed explanation can be found in Klein et al. (2020).

Method

- Select only test cases with $\Delta t_c \geq 100$ms.
- Analyse pressure signals in the liquid part at sensor positions S2, S3 during first cavitation valley: P_{S2}, P_{S3}
- Perform FFT from P_{S2} and P_{S3} and get the three most excited frequencies.
- Display these frequencies in an histogram with a bin width of $\Delta f_{bin} = 10$ Hz. This bin width is chosen, since the resolution of the FFT is the reciprocal of the sample length: $\Delta f_{\text{bin}} = 1/\Delta t_c$.
- The fit function is the sum of n Gauss functions: $g_{\text{fit}}(f) = \sum_{\text{i=1}}^{n} g_i(f)$, where n is the number of modes.

Since the speed of sound and thus the eigenfrequencies vary from test case to test case, the measured frequencies are normalized to $f_{o/o}(1)$ (Eq. 11), which is calculated individually for each test. When using this normalization the bin width must be adjusted. Considering $f_{o/o}(1) \approx 40$ Hz, the adjusted bin width is 0.25.

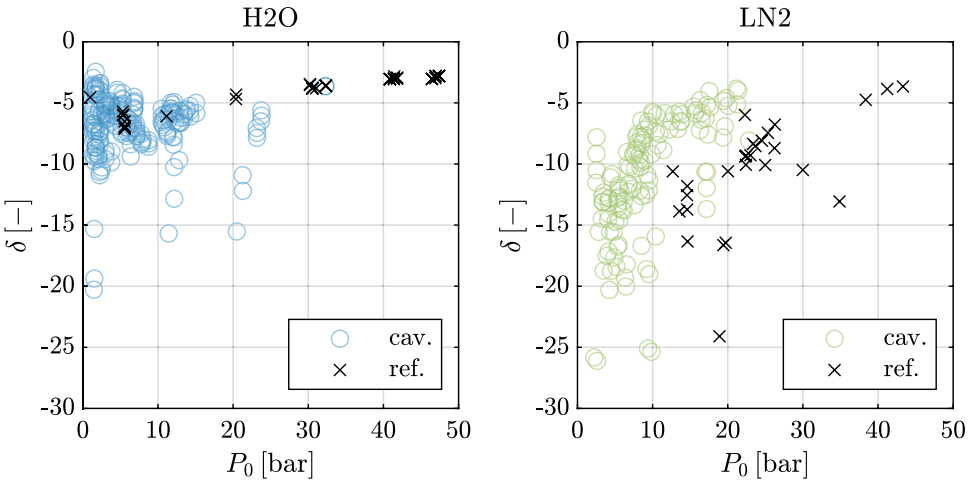

Fig. 20 H_2O, LN2: Decay constant

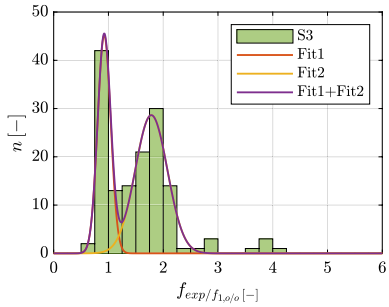

Fig. 21 LN2, S3: Most excited frequencies during first cavitation valley

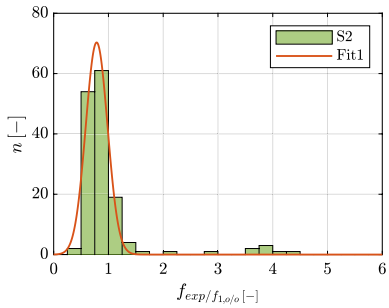

Fig. 22 LN2, S2: Most excited frequencies during first cavitation valley

The results of this method are presented in Fig. 21 (S3) and Fig. 22 (S2). In Fig. 21, the 0.75 - 1 bin and the 1.75 - 2 are the two largest bins. The maxima of the Gaussian fit functions $\max(g_1(f)) = 0.93$ and $\max(g_2(f)) = 1.79$ are close to 1, respectively 2, which is a well matching with $f_{o/o}(i)$.

In Fig. 22, the three bins with the highest count are in the range $0.75 - 1.25$. The Gaussian fit functions maximum is determined to $\max(g_{\text{fit}}) = 0.79$. Considering the bin width of 0.25, this is a good matching with the first eigenfrequency of the pipe open at both ends.

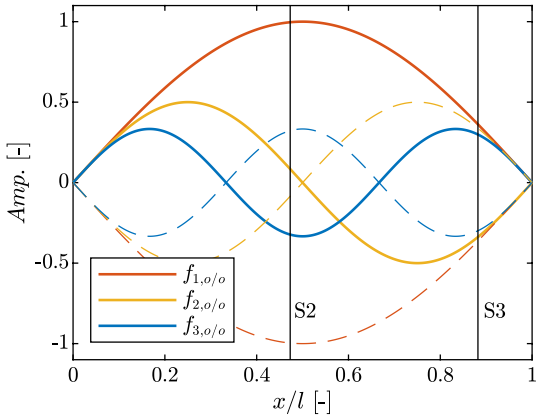

Fig. 23 Standing wave in a tube open at both ends and relative sensor Positions S2 and S3 of the FTTF-2

The difference between both histograms can be explained by regarding Fig. 23, where a standing wave and its overtones in a tube open at both ends are shown. For a better overview, the amplitude of the respective mode is given by $Amp. = 1/n$, where n is the mode number. The relative sensor positions S2 and S3 (FTTF-2) are given. While S3 is far away from any pressure node, S2 is close to the centre pressure node of the second eigenmode. This explains why only the first eigenmode is visible in Fig. 22, while the first two eigenmodes appear in Fig. 21.

In Fig. 24, the first valley of cavitation is shown exemplary for test cases B and F. The pressure traces $P_{\text{S1–S4,dyn}}$, are created by using the dynamic pressure sensors. Since these sensors are only able to measure relative pressure changes, P_0 at the corresponding position is added to the measured signal. The dynamic pressure sensor $P_{\text{S3,dyn}}$ in case B was not working, therefore P_{S3} is plotted instead. While in H_2O more high-frequency features are visible with help of

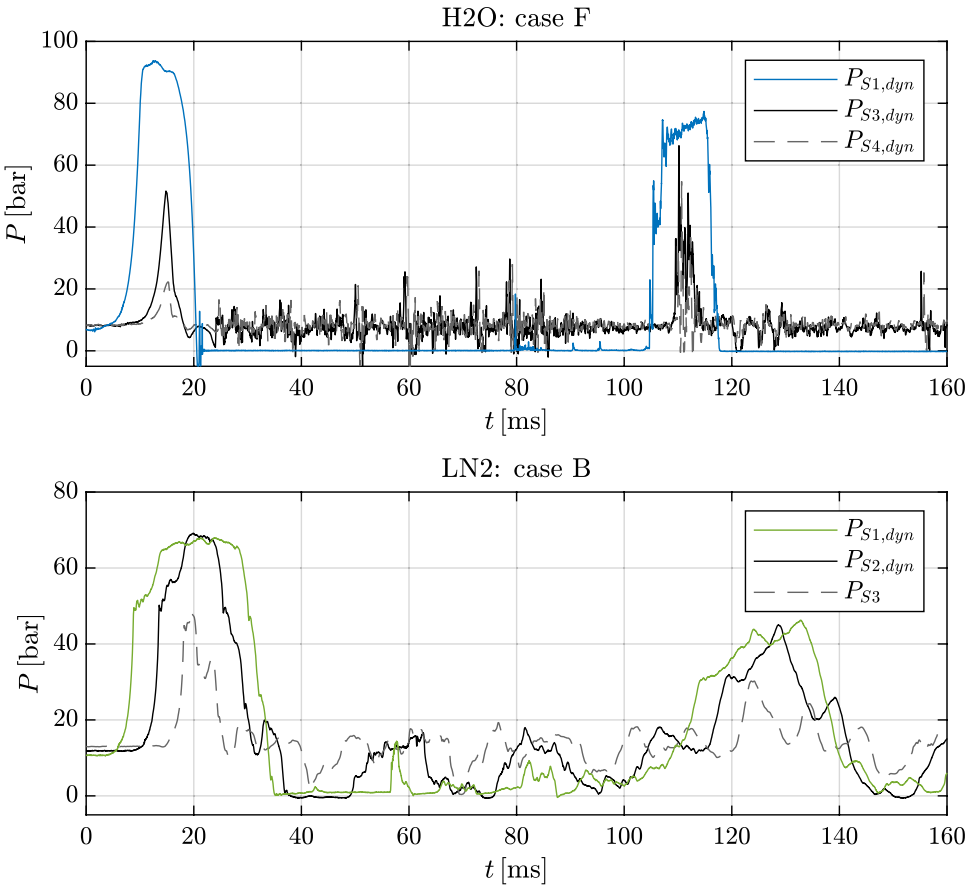

Fig. 24 H_2O/LN2: Pressure traces of tests with cavitation. The first cavitation valley is marked

the dynamic pressure sensors, this difference does not appear in LN2. The pressure curves at position S1 look different in both cases while occurrence of cavitation. In H_2O the pressure is nearly constant during the pressure valley, only a few bumps and a randomly appearing pressure peak can be seen in the second half. Two pressure peaks at position S1 occur in LN2 while cavitation, the distance between these peaks is approximately 27 ms, which coincides well with $f_{1,o/o}$. The pressure traces $P_{\mathrm{S3,dyn}}$ and $P_{\mathrm{S4,dyn}}$ in H_2O are very noisy in contrast to $P_{S2,dyn}$ and $P_{S3,dyn}$ in LN2. As pointed out by Klein et al. (2020) the noise in H_2O is around an order of magnitude larger in H_2O than in LN2.

It is possible to observe the pressure wave in LN2 oscillating between the cavity and the tank directly. $P_{\mathrm{S3,dyn}}$ shows negative pressure peaks, which are alternating with the pressure peaks in $P_{\mathrm{S1,dyn}}$. The pressure curve $P_{\mathrm{S2,dyn}}$ separates these two types of peaks from each other, which make it easy to observe the pressure wave in the pipeline. As shown in Fig. 1, the high-pressure wave is changed to a low pressure wave when it hits the valve, which is a closed end boundary condition. Since the cavity replaces the boundary condition, this transformation does not happen and the pressure wave is oscillating between P_0 and P_v, which is a good agreement with the theory presented in Fig. 3.

In contrast, the pressure wave in the liquid part in H_2O is oscillating at high frequency around P_0. This observation suggests that the cavitation in LN2 forms a more stable acoustic boundary condition than cavitation in H_2O.

While in H_2O it was only possible to find open/open frequencies statistically (Klein et al. 2020), in LN2 these frequencies were also found statistically and the fluid hammer wave during cavitation was observed directly. Combining the findings from the histograms (Figs. 21 and 22), the standing wave (Fig. 23) and the wave tracking (Fig. 24), it is most likely that in LN2 a superposition of the fluid hammer wave, oscillating between the tank and the cavitation, and a standing wave with the frequency $f_{o/o}(2)$ in the liquid part is present.

6 Summary and outlook

Multiple fluid hammer experiments with H_2O and LN2 were performed at the FTTF at DLR Lampoldshausen. The results of these experiments were presented and compared to each other. Firstly the agreement with the Joukowsky pressure was shown for a wide range of static pressure for both fluids. Then the influence from cavitation on the frequency

was investigated. It has been found that the occurrence of cavitation lowers the frequency of the pressure oscillation in both fluids after the cavitation disappeared. The cavitation duration were measured and compared with the estimations of Wylie et al. (1993) and Prasser et al. (1998). While the measurements in both fluids were below the prediction of Wylie et al. (1993), the prediction of Prasser et al. (1998) was found to be more accurate.

It was shown statistically that the cavitation in LN2 acts as an open end boundary condition, which confirms the results from Klein et al. (2020) made with H_2O. Furthermore the pressure wave in LN2, unlike in H_2O, was tracked directly and showed good agreement with theory. Since a standing wave was found with the use of histograms, it is suspected that in LN2 a superposition of the fluid hammer wave oscillating between the cavitation and the valve and a standing wave in the liquid part is present.

In future experiments an optical access will be installed close to the valve, so that the flow structure during the cavitation growth can be observed using a high speed camera and the nature of the observed reproducible pressure oscillations during the period of cavitation can be clarified.

Acknowledgements The authors greatly acknowledge the support of the M3 test facility team and Yannik Miene during the test campaign.

Funding Open Access funding enabled and organized by Projekt DEAL. This research received no specific grant from any funding agency, commercial or not-for-profit sectors.

Declarations

Conflict of interest The authors report no conflict of interest.

References

Barna IF, Imre AR, Baranyai G et al (2010) Experimental and theoretical study of steam condensation induced water hammer phenomena. Nucl Eng Des 240(1):146–150

Bergant A, Simpson A, Tijsseling A (2006) Water hammer with column separation: a historical review. J Fluids Struct 22(2):135–171. https://doi.org/10.1016/j.jfluidstructs.2005.08.008

Bombardieri C, Traudt T, Manfletti C (2014) Experimental and numerical analysis of water hammer during the filling process of pipelines. In: Space Propulsion Conference, Cologne, Germany

Bonin C (1960) Water-hammer damage to Oigawa power station. J Eng Power 10(1115/1):3672721

Gibek I, Maisonneuve Y (2005) Waterhammer tests with real propellants. In: 41st AIAA/ASME/SAE/ASEE Joint Propulsion Conference & Exhibit, p 4081

Giot M, Prasser HM (2004) Two-phase flow water hammer transients and induced loads on materials and structures of nuclear power plant (wahaloads). In: FISA-2003

Gouriet J, Huertas-Martinez A, Buchlin J, et al (2016) Multiphase fluid hammer with cryogenic fluids. In: Proceedings of Space Propulsion

Graf T, Fischer H, Reul H et al (1991) Cavitation potential of mechanical heart valve prostheses. Int J Artif Organs 14(3):169–174

Joseph J, Agrawal G, Agarwal D et al (2017) Fluid-hammer induced pressure oscillations in a cryogenic feed line. In: IOP Conf Ser: Mater Sci Eng 171 012049. https://doi.org/10.1088/1757-899x/171/1/012049

Joukowsky N (1900) Über den hydraulischen Stoss in Wasserleitungsrohren. Académie impériale des sciences de St. Pétersbourg in German 9(8):5

Klein S, Traudt T, Bombardieri C, et al (2018) Influence of static pressure on the damping of pressure waves in rocket engine feed lines. In: Proceedings-13th International Conference on Pressure Surges

Klein S, Traudt T, Bombardieri C, et al (2019) Damping of water hammer with cavitation in rocket engine feed lines. In: 32nd International Symposium on Space Technology and Science

Klein S, Traudt T, Oschwald M (2020) Influence of cavitation on the acoustic boundary conditions in water hammer experiments. In: 18th International Symposium on Transport Phenomena and Dynamics of Rotating Machinery, ISROMAC

Klein S, Traudt T, Oschwald M (2021) Comparison between water and liquid nitrogen pressure surge experiments to analyze cavitation induced noise growth. In: 11th International Symposium on Cavitation

Korteweg D (1878) Ueber die fortpflanzungsgeschwindigkeit des schalles in elastischen röhren. Ann Phys 241(12):525–542

Lardier C (2018) The soviet manned lunar program n1–l3. Acta Astron 142:184–192. https://doi.org/10.1016/j.actaastro.2017.10.007

L'Hullier V (2009) Propulsion in the atv spacecraft system-lessons learnt. In: 45th AIAA/ASME/SAE/ASEE Joint Propulsion Conference & Exhibit, p 4900

Li W, Gao Z, Jin Z, Qian J (2020) Transient study of flow and cavitation inside a bileaflet mechanical heart valve. Appl Sci 10(7):2548

Prasser HM, Zschau J, Böttger A (1998) Entwicklung von zweiphasenmesstechnik für vergleichende untersuchungen zur beschreibung von transienten strömungen in rohrleitungen. Abschlussbericht zum BMBF-Vorhaben Nr 11ZF9504/1

Skudrzyk E (2012) The foundations of acoustics: basic mathematics and basic acoustics. Springer, New York

Traudt T, Bombardieri C, Manfletti C (2015) High speed imaging of water hammer with column separation. In: Pressure Surge Conference, Dublin

Traudt T, Bombardieri C, Schleicher E, et al (2016) Investigation of pressure hammer with wire mesh sensor and high speed imaging techniques. In: Space Propulsion Conference, Rome, Italy

Wilson PS, Roy RA (2008) An audible demonstration of the speed of sound in bubbly liquids. Am J Phys 76(10):975–981

Wylie EB, Streeter VL, Suo L (1993) Fluid transients in systems, vol 1. Prentice Hall Englewood Cliffs, Englewood Cliffs

Zielke W, Perko H (1985) Unterdruckerscheinungen und druckstoβ berechnung. 3R Int 24(7):348–355